

RESEARCH

Open Access



# Robust ternary system of corncob-derived carbon quantum dots/ ZnFe<sub>2</sub>O<sub>4</sub>/graphene oxide for wastewater treatment

Wajeeha Qayyum<sup>1</sup>, Noor Tahir<sup>1</sup>, Muhammad Zahid<sup>1\*</sup>, Saima Noreen<sup>1</sup>, Muhammad Yaseen<sup>2</sup>, Abeer A. AlObaid<sup>3</sup>, Qamar Abbas<sup>4</sup> and Ghulam Mustafa<sup>5</sup>

## Abstract

Water contamination emerging from urban and industrial waste disposal is posing an alarming threat to human and marine life. Hence, it is imperative to take a crucial approach to lowering the overall cost and time of wastewater treatment. The efficiency of heterogeneous photo Fenton green wastewater treatment processes relies mainly on the morphology and surface interface properties of photocatalysts for harnessing maximum sunlight energy. This research work reports for the first time the hydrothermal synthesis of ternary zinc ferrite coupled with carbon quantum dots derived primarily from corncob biomass and supported over graphene oxide. The physiochemical properties and microstructure of magnetic graphene oxide anchored over carbon quantum dots included Fourier Transform Infrared Spectroscopy, Scanning Electron Microscope/Energy Dispersive X-ray, X-ray photoelectron spectroscopy, X-ray diffraction and Ultraviolet–Visible Spectroscopy. The effect of several factors on the photocatalytic degradation of Rhodamine B (RhB) dye was studied and maximum degradation was attained at optimized conditions of pH=4, catalyst concentration (20 mg/100 mL), oxidant dose (10 mM) and degradation time (60 min). Response surface methodology was used to determine the optimization of various interacting parameters. The current research focused on the utilization of waste corncob biomass as a potential candidate for the novel ternary nanocomposite for effective treatment dye wastewater and reuse of treated dye water over wheat seeds germination.

**Keywords** Biomass, Dye degradation, Advance oxidation process, Carbon quantum dots, Metal ferrite, Toxicity removal

## Introduction

Water comprises a significant proportion of the terrestrial globe. Approximately 98% of the total water volume consists of seawater, rendering it unsuitable for potable consumption due to its elevated salinity levels. According to scientific research, it has been determined that approximately 2% of the Earth's water resources are classified as potable, suitable for human consumption [1]. The proliferation of organic pollutants from worldwide industrialization, commercialization, and agricultural practices has resulted in significant contamination of freshwater reservoirs [2]. Therefore, water pollution has arisen as a prominent worldwide environmental dilemma. Discharging

\*Correspondence:

Muhammad Zahid  
rmzahid@uaf.edu.pk

<sup>1</sup> Department of Chemistry, University of Agriculture, Faisalabad 38040, Pakistan

<sup>2</sup> Department of Physics, University of Agriculture, Faisalabad, Pakistan

<sup>3</sup> Department of Chemistry, College of Science, King Saud University, Riyadh, Saudi Arabia

<sup>4</sup> Institute of Chemistry and Technical electrochemistry, Poznan University of Technology, 60965 Poznan, Poland

<sup>5</sup> Department of Chemistry, University of Okara, Okara, Pakistan



© The Author(s) 2025. **Open Access** This article is licensed under a Creative Commons Attribution-NonCommercial-NoDerivatives 4.0 International License, which permits any non-commercial use, sharing, distribution and reproduction in any medium or format, as long as you give appropriate credit to the original author(s) and the source, provide a link to the Creative Commons licence, and indicate if you modified the licensed material. You do not have permission under this licence to share adapted material derived from this article or parts of it. The images or other third party material in this article are included in the article's Creative Commons licence, unless indicated otherwise in a credit line to the material. If material is not included in the article's Creative Commons licence and your intended use is not permitted by statutory regulation or exceeds the permitted use, you will need to obtain permission directly from the copyright holder. To view a copy of this licence, visit <http://creativecommons.org/licenses/by-nc-nd/4.0/>.

wastewater from industrial processes and diverse human activities has led to significant and hazardous ecological consequences. A concerning demographic is experiencing daily hardships due to the lack of access to potable water. The gross negligence exhibited by multiple industrial units in releasing untreated wastewater into freshwater streams has presented significant risks to human health [3].

Insufficient mineralization of contaminants emerged as a prevalent issue when using traditional techniques, including filtration, extraction, ultrafiltration, oxidation, activated carbon adsorption, chemical oxidation, electrolysis, and biological treatment. Continuous investigation into the advancement of diverse oxidation technologies has successfully addressed the limitations associated with previous methods [4]. During the early 1980s, the potential use of advanced oxidation processes (AOPs) for water treatment and purification was unveiled. The hydroxyl radical, a potent oxidizing agent, is used in wastewater treatment to facilitate the degradation of intricate organic pollutants into less harmful molecules [5]. Fenton reaction, sonolysis, heterogeneous photocatalysis, ozone treatment, catalytic moist air oxidation, and electrochemical oxidation represent a range of advanced oxidation processes. Occasionally, these systems exhibit collaborative behavior, resulting in the generation of potent oxidizing radicals. These radicals effectively target and neutralize waterborne pollutants, transforming them into less harmful substances like carbon dioxide, water, and inorganic ions. Various semiconductor photocatalysts, including binary or ternary metal oxides supported on carbon-based materials, may be used in advanced oxidation processes [6].

By harnessing the reactivity of hydroxyl radicals ( $\cdot\text{OH}$ ) generated through a Fenton reaction, the removal efficiency of these contaminants can be significantly enhanced compared to conventional physicochemical and biological methods employed in wastewater treatment [7]. The conventional Fenton reaction entails the activation of hydrogen peroxide ( $\text{H}_2\text{O}_2$ ) using ferrous ions ( $\text{Fe}^{2+}$ ) to generate hydroxyl radicals ( $\cdot\text{OH}$ ). However, the efficiency of  $\text{Fe}^{2+}$  regeneration is typically low [8]. Ultraviolet (UV) radiation has been successfully employed in the Fenton process to augment the recycling of  $\text{Fe}^{2+}/\text{Fe}^{3+}$  ions [9]. Nevertheless, several limitations exist regarding the practical application of the homogeneous photo-Fenton technique [10]. In the context of solar energy, it is noteworthy that ultraviolet (UV) radiation constitutes merely 5% of the total solar energy spectrum. Harnessing UV light necessitates an extremely acidic milieu and yields the formation of iron sludge as a byproduct [11]. To overcome these challenges, the Vis-light/catalyst/ $\text{H}_2\text{O}_2$  system underwent modifications to implement

a heterogeneous photochemical approach to eliminate organic pollutants. Scientists are, therefore, intrigued by the prospect of developing visible light-assisted Fenton-like catalysts [12, 13].

Semiconductors and magnetic materials, alongside other materials, have been extensively investigated as prospective photocatalysts. The metals and organic compounds have also been successfully removed/extracted from the wastewater samples [14–17]. A demand exists for a material exhibiting optimal degradation efficiency, yet no existing product in the market fulfills this requirement. Various types of materials, including nanoparticles made of semiconductors and oxides, are currently being investigated to enhance the efficiency of photocatalysis [18, 19]. As an oxide-based material, ferrites are synthesized for photocatalysis applications due to their magnetic properties, ability to utilize a wide range of the solar spectrum, and electrical and optical characteristics [11]. Comparably, semiconductor materials, such as metal oxide, exhibit substantial influence in photocatalysis. The bandgap energies of these semiconductors can be altered without altering the material composition by manipulating particle size and shape [20].

The kind of catalyst and its surface characteristics have a big impact on the photocatalysis process. The main prerequisites are the capacity to absorb a wide range of sunlight, the efficient separation of charge carriers over the catalyst's surface, and the contribution of charges at interfaces to redox processes making ferrites ideal candidates for wastewater treatment [21]. Investigating zinc ferrite ( $\text{ZnFe}_2\text{O}_4$ ) as a photocatalyst is motivated by its reduced bandgap energy and enhanced magnetic properties compared to other ferrites [22]. Nevertheless, zinc ferrites exhibit limitations that hinder their effectiveness, such as rapid recombination of electron/hole pairs, susceptibility to photo-corrosion, and inferior photostability [23]. The enhancement of ferrite performance was achieved through the implementation of heterojunction architectures, wherein they were integrated with additional semiconductor materials [24].

Heterogeneous photocatalysis, which uses semiconductor materials based on metal oxides to break down persistent pollutants, has gained popularity. Carbon quantum dots, a novel carbon-based photocatalyst, have arisen in traditional semiconductor materials. Carbon quantum dots (CQDs) have gained significant attention recently as an unknown category of nanomaterials with zero-dimensional characteristics [25]. They are highly regarded as promising for interfacial regulation due to their inherent properties of up-conversion photoluminescence, exceptional electron-transfer capability, and favorable biocompatibility [26]. There are several potential uses for CQDs in water purification

and environmental remediation due to their remarkable characteristics [27]. The most promising carbon sources for the manufacture of water-soluble carbon quantum dots have lately been found in natural waste materials, particularly green waste [28]. Hydrothermal, chemical oxidation, solvothermal, carbonization, and microwave-assisted synthesis are some of the most popular methods for the facile synthesis of carbon quantum dots (CQDs) from natural sources, according to the literature. These methods are known for their rapid synthesis processes and straightforward fabrication [29].

Another important challenge is discovering optimal methods to enhance the synergistic interaction between biomass carbon quantum dots electron transfer capability and super magnetic zinc ferrite's crystal surface properties. Conventional impregnation or adsorption methods may cause carbon quantum dots to be haphazardly attached. Some investigations have shown that photoinduced electrons and holes from a photocatalyst with strong redox capabilities may be spatially dispersed across crystal surfaces when exposed to light [6]. Thus, using a light-induced synthesis process like photo-deposition to incorporate biomass carbon quantum dots as electron acceptors onto zinc ferrite (ZFO) crystal surfaces is new and useful [30].

In addition, the fabrication of magnetic zinc ferrites-based heterojunction photocatalysts can address the recombination of photogenerated charges and enhance the capabilities of separation and regeneration by utilizing an external magnetic field, thus making it suitable for practical applications [31]. The primary constituents of magnetic materials are ferrites ( $\text{MnFe}_2\text{O}_4$ ,  $\text{CoFe}_2\text{O}_4$ ,  $\text{ZnFe}_2\text{O}_4$ ), metal oxides ( $\text{Fe}_3\text{O}_4$ ,  $\text{Co}_3\text{O}_4$ ,  $\text{Mn}_3\text{O}_4$ ,  $\gamma\text{-Fe}_2\text{O}_3$ ), and elemental metals ( $\text{Fe}^0$ , Co) [26, 32].

Furthermore, optimizing the synergistic interaction between the electron transfer capability of biomass carbon quantum dots (CQDs) and the crystal surface properties of zinc ferrite (ZnFe) presents a noteworthy challenge that merits additional investigation. Utilizing conventional impregnation or adsorption techniques may lead to a haphazard dispersion and precarious attachment of Carbon quantum dots. However, certain studies have indicated that a photocatalyst's photoinduced electrons and holes, possessing potent redox capabilities, can be spatially distributed across distinct crystal planes when exposed to light irradiation [30, 33, 34]. Graphene oxide is a highly effective support material and electron reservoir in ternary heterojunctions, as it can capture electrons from metal oxides [35, 36]. The inhibition of charge carrier recombination leads to an enhancement in photo-response and an increase in the stability of hybrid materials for their diverse range of applications [37].

The current research investigation involves the synthesis of carbon quantum dots/  $\text{ZnFe}_2\text{O}_4$  anchored on graphene oxide ternary heterojunction. The novel nanocatalyst was synthesized for the first time, as far as our current understanding goes, and its photocatalytic performance was evaluated for the degradation of Rhodamine B dye when exposed to UV light. The primary focus was the advancement of a photocatalyst that exhibited enhanced photocatalytic performance when exposed to ultraviolet (UV) radiation. A variety of analytical methods, including Scanning Electron Microscopy with Energy Dispersive X-ray Spectroscopy (SEM-EDS), X-ray Diffraction (XRD), X-ray photoelectron spectroscopy (XPS), Ultraviolet-Visible Spectroscopy (UV-Visible), and Fourier Transform Infrared Spectroscopy (FT-IR), were employed to conduct a comprehensive analysis of the composite material. The composite material's photocatalytic efficacy was assessed by optimizing many parameters, such as catalyst dosage, pH level, oxidant dose, reaction duration, and initial dye concentration. The catalytic efficacy of ternary Carbon quantum dots-zinc ferrite-graphene oxide (CZG) nanocomposite was compared with its binary counterparts, zinc ferrite-graphene oxide (ZG) and CQDs/Zinc ferrite (CZ). The present study has shown a notable synergistic effect between carbon quantum dots and magnetic graphene oxide catalysts, resulting in a substantial improvement in the photocatalytic efficiency upon exposure to Ultraviolet radiation. The toxicity analysis was also done by checking the toxicity of treated dye wastewater by ternary CZG composite on wheat seeds.

## Experimental

### Materials and reagents

Sodium Nitrate ( $\text{NaNO}_3$ , >99%), Potassium Permanganate ( $\text{KMnO}_4$ , >99%), Iron Nitrate Nonahydrate ( $\text{Fe}_2(\text{NO}_3)_9 \cdot 9\text{H}_2\text{O}$ , >99%), Sulfuric Acid ( $\text{H}_2\text{SO}_4$ , 98%), Hydrogen Peroxide ( $\text{H}_2\text{O}_2$ , 35w/w %), ethanol ( $\text{CH}_3\text{CH}_2\text{OH}$ , 95.6%), Zinc Nitrate Nonahydrate ( $\text{Zn}(\text{NO}_3)_2$ ) and Acetic Acid were purchased from Sigma Aldrich (USA). The dye Rhodamine B was procured from the Fischer Scientific company. The graphite powder was acquired from Scharlau (Spain). Iron nitrate Nonahydrate ( $\text{Fe}(\text{NO}_3)_2 \cdot 9\text{H}_2\text{O}$ , 98%) was received from Unichem. Sodium Nitrate and potassium permanganate were obtained from Merck, a reputable supplier of chemical compounds. All the compounds utilized in the experiment were of analytical grade, and no additional purification procedures were conducted before their application. During the research investigation, distilled water was used to perform all chemical reactions.

### Synthesis of graphene oxide (GO) and carbon quantum dots (CQDs)

GO was synthesized by the modified Hummers method [38]. Carbon quantum dots (CQDs) were synthesized by a method reported earlier [39]. The hydrothermal technique is used to synthesize supermagnetic  $\text{ZnFe}_2\text{O}_4$  nanoparticles [40].

### Synthesis of binary nanocomposites

Hydrothermal treatment was employed to synthesize the  $\text{ZnFe}_2\text{O}_4$ /Graphene oxide (ZG) binary composite as reported [41]. Graphene dispersion was sonicated to get a clear suspension. The slow addition of this cleared suspension of GO was mixed in the solution of zinc ferrite. Zinc ferrite-carbon quantum dots, a binary composite, were prepared by the same method as graphene oxide/ $\text{ZnFe}_2\text{O}_4$  formed [42].

### Synthesis of ternary CQD/ $\text{ZnFe}_2\text{O}_4$ /GO nanocomposite (CZG)

In-situ hydrothermal method was prepared for the novel ternary composite CZG. The graphene dispersion was subjected to sonication to achieve a homogeneous

and transparent suspension. The gradual introduction of this clarified suspension of graphene oxide was combined with the zinc ferrite solution. After some time, an appropriate amount of Carbon quantum dots suspension was added to the zinc ferrite solution under continuous magnetic stirring. The above solution was autoclaved at a specific temperature for several hours. After that, the product was cooled down and dried in an oven. A schematic description of ternary nanocomposite synthesis is presented in Fig. 1

### Characterization and equipment

Morphology, elemental analysis, and microstructure of as-produced ternary CZG were characterized using a scanning electron microscope with energy dispersive spectroscopy (EDS; FEI NOVA 450 NANOSEM). Each powder sample was analyzed by XRD (operated by Bruker D8 Advanced instruments) to determine its crystalline properties throughout a range of 2 values, from 5 to 80 degrees. Thermo Nicolet's Fourier Transform Infrared Spectrometer can detect the presence of several functional groups on the surfaces of produced photocatalysts. The bandgap of the produced

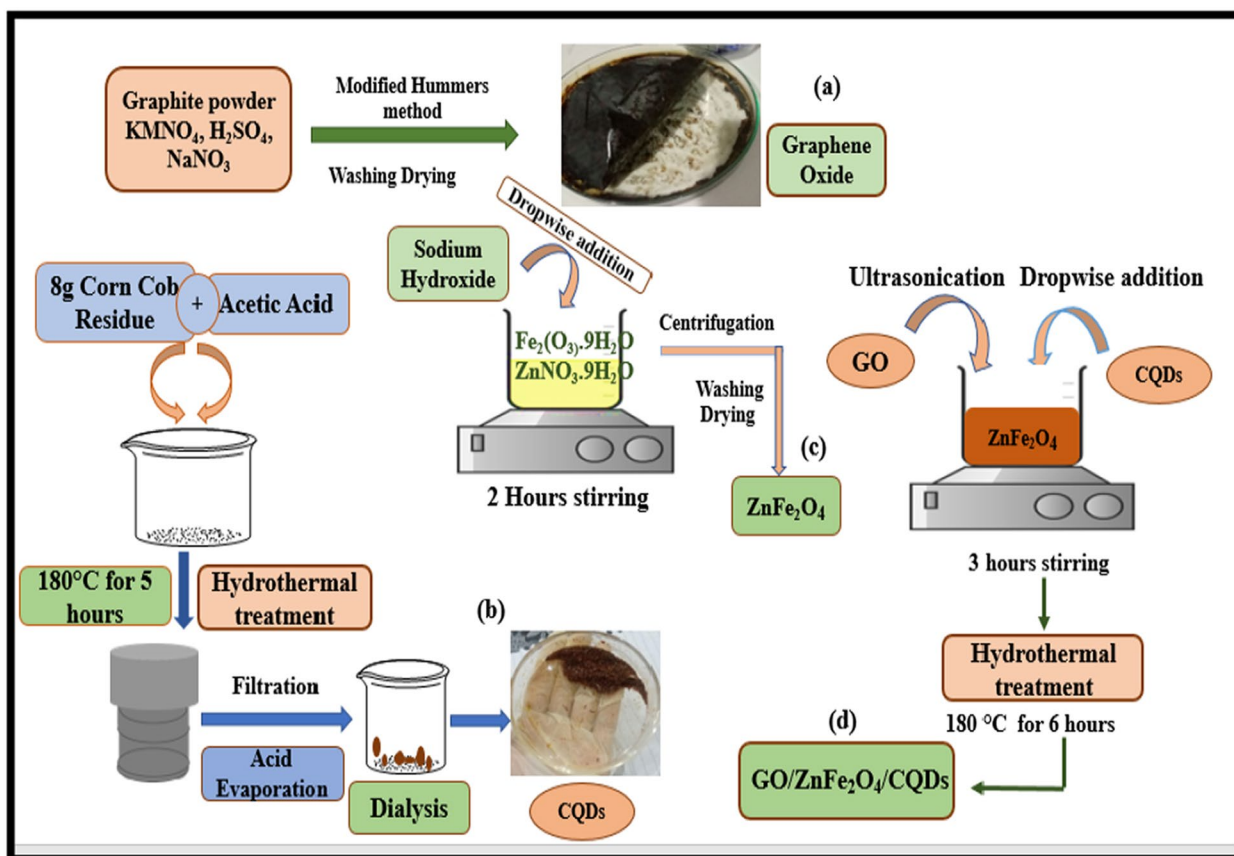


**Fig. 1** Schematic diagram of synthesis ternary composite (CZG): Synthesis of (a) GO, (b) CQDs, (c)  $\text{ZnFe}_2\text{O}_4$  and (d)  $\text{GO}/\text{ZnFe}_2\text{O}_4/\text{CQDs}$

composites was determined by analyzing their absorption spectrum between 200 and 800 nm using a UV–VIS spectrophotometer (Cecil CE 7200). The several elemental states of surface groups were examined via X-ray Photoelectron Spectroscopy (XPS system, Escalab-250 Thermo scientific, UK).

#### Analysis of photocatalytic pollutant degradation

Photocatalytic degradation of the cationic dye Rhodamine B under UV light conditions was used to compare the photocatalytic performance of hybrid ternary and binary composites. The deterioration was carried out under normal atmospheric conditions, with ultraviolet light as the principal illumination source. Feasibility degradation experiments were performed with 100 mL RhB dye solutions, with an initial dye concentration of 10 ppm and a catalyst loading of 20 mg, with pH 3, 7 and 9. Ultra-sonication of the fluid for about 15 min disseminated the nanoparticles. After letting the suspension sample sit in the dark for approximately thirty minutes, we exposed it to sunlight. The solution was continually agitated throughout the procedure to achieve absolute adsorption–desorption equilibrium. An adsorption–desorption equilibrium must first be established to attain efficient adsorption of certain pollutants onto the surface of photocatalysts. The solution was left in the UV chamber while continuously shaken in an orbital shaker. After regularly centrifuging a 10 mL sample at 6000 rpm to separate its components, the absorbance of the solution may be determined. Using a double-beam spectrophotometer set to a wavelength of 554 nm, the concentration of RhB in the supernatant liquid was calculated. A control experiment was performed without a catalyst in each trial for the optimization of RhB degradation with CZG catalysts. This control experiment further confirmed the lack of any noticeable catalytic activity under the influence of UV light or in the absence of a catalyst. We used the formula mentioned in Eq. 1 to compare the decline in activity of CZG, ZG, and CZ catalysts.

$$\% \text{ Degradation} = 1 - \frac{A}{A_0} \times 100 \quad (1)$$

The initial absorbance, denoted by ( $A_0$ ), is described by Eq. (1), and  $A$  is linked to absorbance measured after irradiation of solution under ultraviolet light. For this purpose, we used a solar power meter (SM206) and a light meter (HS1010A). Under identically optimized circumstances the photocatalyst was recycled five times to test the catalyst's photostability.

### Comprehensive characterization analysis of binary (CZ, ZG) and ternary (CZG) nanocomposites

#### FT-IR analysis

The identification of functional groups on the catalyst surface is done using the Fourier Transform Infrared spectroscopy approach. Figure 2 shows the FTIR data obtained for the samples. FT-IR spectra in the frequency range of  $4000 \text{ cm}^{-1}$  to  $500 \text{ cm}^{-1}$  were used to characterize the surface functional groups of CQDs. O–H bonds are readily visible in the Fourier Transform Infrared spectrum when the peak at  $3420 \text{ cm}^{-1}$  is considered because of its significant vibration frequency [43]. Furthermore, the peak characteristics of the C–H, C=O, and C=C groups correspondingly demonstrate the tunable frequencies of  $2900 \text{ cm}^{-1}$ ,  $1700 \text{ cm}^{-1}$ , and  $1625 \text{ cm}^{-1}$ .

Additionally, a frequency of  $1427 \text{ cm}^{-1}$  may be used to detect C–N functional groups [44]. The GO-ZnFe<sub>2</sub>O<sub>4</sub> spectra demonstrate that GO's oxygen function group peaks are significantly diminished or vanished, and new bands for GO-ZnFe<sub>2</sub>O<sub>4</sub> emerged at around  $544 \text{ cm}^{-1}$  and  $423 \text{ cm}^{-1}$ . The tetrahedral Zn<sup>2+</sup> (Zn–O mode) stretching vibration is responsible for the band at  $544 \text{ cm}^{-1}$ , while the octahedral Fe<sup>3+</sup> (Fe–O mode) stretching vibration is responsible for the band at  $500 \text{ cm}^{-1}$  [45].

#### XRD analysis

The crystalline size of the nanocrystal can be determined by using XRD. The XRD patterns of binary and ternary composites are shown in Fig. 3. Graphene oxide's distinctive peaks at  $2\theta = 10.3^\circ$  and  $13.2^\circ$  corresponds to the crystal planes (001) and (002), indicating that graphite was successfully oxidized. The observed distinctive peaks at  $2\theta$  of  $29.9^\circ$ ,  $35.2^\circ$ ,  $42.9^\circ$ ,  $53.2^\circ$ ,  $56.5^\circ$ , and  $64.2^\circ$  are assigned to the crystal planes of (220), (311), (400), (422), (511), and (440) (JCPDS card No. 89–1010), and are used to determine the cubic spinal structure of ZnFe<sub>2</sub>O<sub>4</sub>.

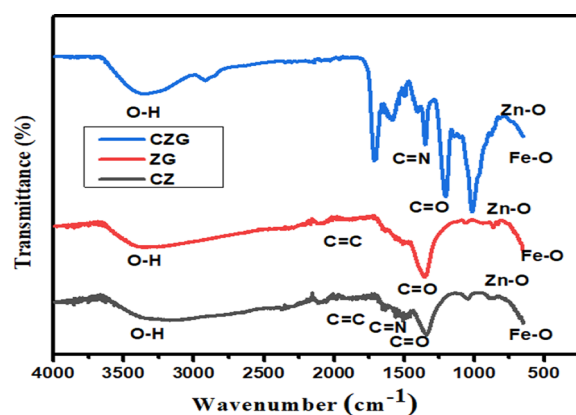


**Fig. 2** FTIR analysis of CZG, ZG and CZ nanocomposites

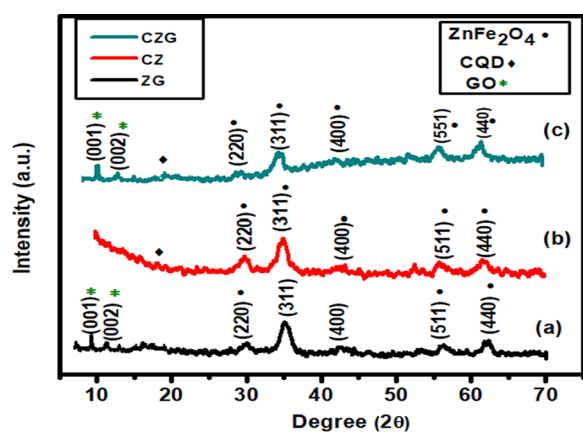


**Fig. 3** FTIR and XRD analysis of **a** CZG, **b** CZ, **c** ZG

Furthermore, both pure ZnFe in GO-ZnFe<sub>2</sub>O<sub>4</sub> are effectively generated based on the high-intensity diffraction peaks. ZnFe and ZG were found to have typical grain sizes of 23.5 nm and 22.9 nm, respectively [46].

Carbon Quantum Dots crystal structures are seen in the XRD patterns. Since the intense diffraction peak value at 22.8° coincides with the interlamellar spacing of the graphite structure, CQDs may be referred to as the degree (002) planes of graphite [47]. Although the slightly sharp peak reveals a less amorphous nature of carbon, the peak at 19.2° with a d-spacing of 0.30 nm is attributed to carbon. No other appearance of the CQD peak was observed because of the low concentration and majorly high distribution in the ternary sample. The drop in peak intensity in the ternary CZG composite is associated with metal ferrites confirming the presence of iron nitrate in the composite as well as the incorporation of various functional groups in the ternary hybrid [48]. The crystallite size of binary and ternary nanocomposites is calculated using Debye Scherrer equation

$$D = K\lambda/\beta \cos \theta \quad (2)$$

In Eq. (2), (D) is the nanoparticle's crystallite size, is the X-ray wavelength (0.154 nm and K is the Scherrer constant with a value of 0.94, and), is FWHM (full width at half maximum), and the diffraction angle is labelled as (θ). The Scherrer equation yielded crystallite sizes of 27.8 nm, 24.65 nm, and 12.65 nm for CZG, ZG, and CZ, respectively. The nonexistence of any additional peak also corresponds to the purity of the synthesized nanocomposite.

#### SEM-EDS analysis

Scanning electron microscopy was used for the determination of morphologies of nanoparticles. The spinel cubic structure of zinc ferrite can be identified

based on the information provided [49]. The SEM-EDS images of binary and ternary nanocomposites are shown in Fig. 4. The morphology of the ZnFe<sub>2</sub>O<sub>4</sub> (ZnFe) particles transformed a cubic system to an agglomerated random form as the concentration of graphene oxide (GO) and carbon quantum dots was increased. Assemblies of several entangled spherical-like nanostructures of quantum dots distributed across stacked graphene sheets were seen in the ternary hybrid formed when CQDs were combined with ZnFe<sub>2</sub>O<sub>4</sub> and GO. The clustering phenomenon observed in the zinc ferrite samples could be attributed to the magnetic properties exhibited by the material. Due to the inherent magnetic characteristics exhibited by zinc ferrite, it is plausible for the particles to experience a decline in their colloidal stability, leading to their mutual absorption and subsequent aggregation. Composite formation was observed through a swift morphological shift from cubic to randomly agglomerated particles.

Elemental analysis of the prepared sample was taken from EDS spectra. Zn, Fe, O, and C show composite preparation in relative weight percentages.

#### XPS analysis

The chemical composition and the surface chemical states of all binary and ternary nanocomposites were analyzed using X-ray photoelectron spectroscopy (XPS). The survey spectra of ZG, CZ, and CZG nanocomposites are shown in Fig. 5. All of the samples displayed distinctive peaks at C1s (285.4 eV), O1s (530.2 eV), Fe2p3 (724.3 eV), Zn2p3 (1021.2) and peak Zn2p1 (1044.8 eV). In the XPS spectra of the ternary CZG nanocomposite, the significant relative peaks of C1s, O1s, Fe2p3, Zn2p1, and Zn2p3 were observed to move towards the higher binding energies. This suggests the successful combining of all components in the ternary heterostructures. The distinctive C1s peak indexed at binding energy (285.4 eV) is attributed to adventitious carbon. The peak arising at binding energy 530.2 eV is related to O1s, suggesting a normal oxygen signal in the hydroxyl group on surface. The distinctive peaks of Zn2p3 and Zn2p1 were found at binding energies of 1021.2 eV and 1044.8 eV, respectively. These values show that Zn and Zn<sup>2+</sup> ions were formed in the nanocomposites [42]. The binding energies of 711 eV and 724.8 eV are related to Fe<sup>3+</sup> satellite peaks corresponding to Fe2p1 and Fe2p3 peaks consequently indicating the presence of Fe<sup>2+</sup> and Fe<sup>3+</sup> oxidation states. The relative atomic percentages of C1s, O1s, Fe2p3, and Zn2p3 in ternary CZG are 3.2%, 79.4%, 14.4%, and 3.0%. The relative atomic percentages of C1s, O1s, Fe2p3, and Zn2p3 in binary CZ nanocomposite are 21.1%, 64.5%, 3.5%, 10.9% whereas these percentages in

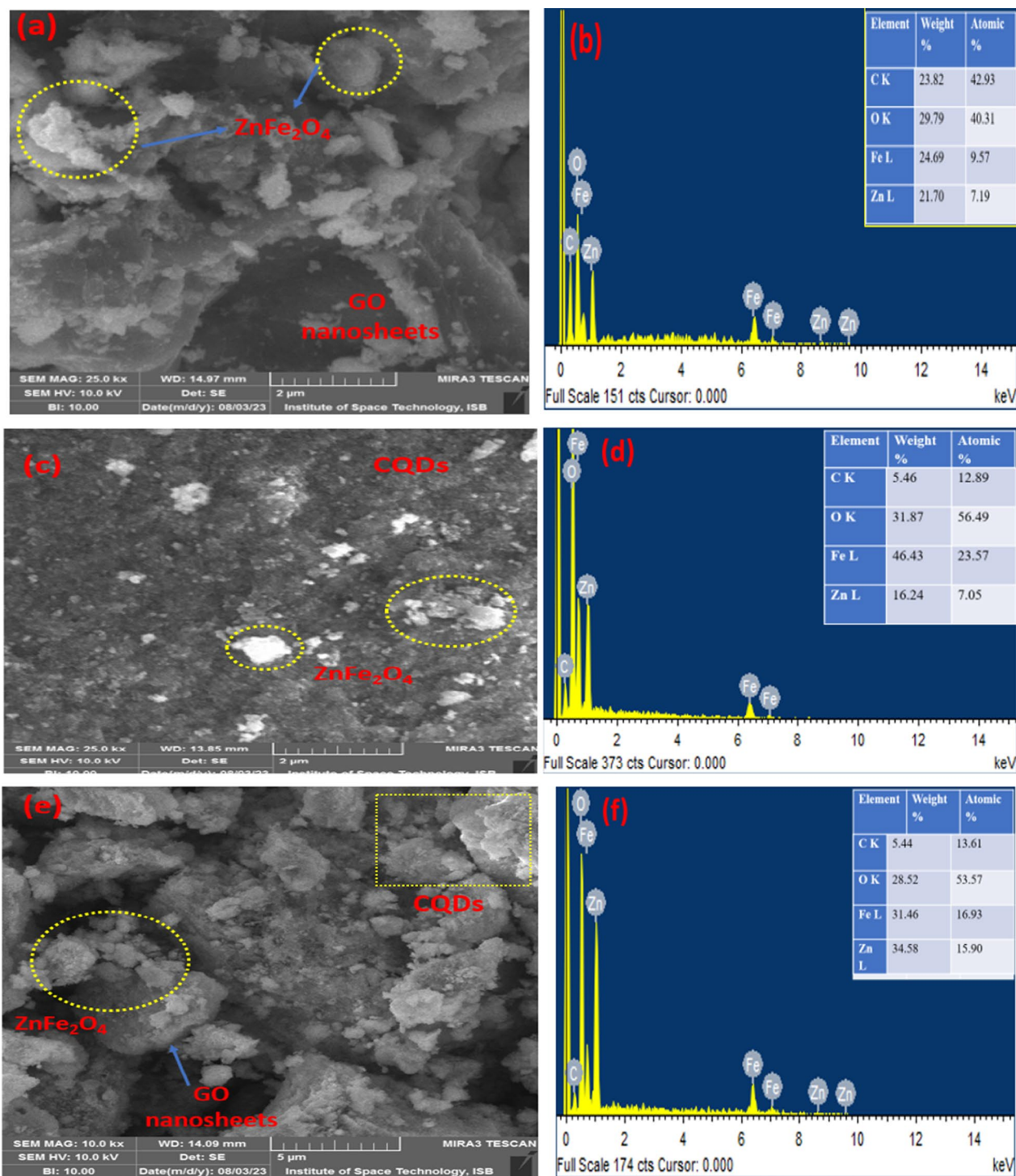


**Fig. 4** SEM-EDS images of (a & b) ZG (c & d) CZ (e & f) CZG

other binary (ZG) are 33.3%, 53.4%, 1.5% and 11.8% for C1s, O1s, Fe2p3, and Zn2p3 respectively. Hence, Above all characterization techniques along with XPS can be utilized to attain a better understanding of how these

three components interacted leading to the final design of ternary heterostructure and surface phenomena occurring at the interface leading to the photodegradation process [50].

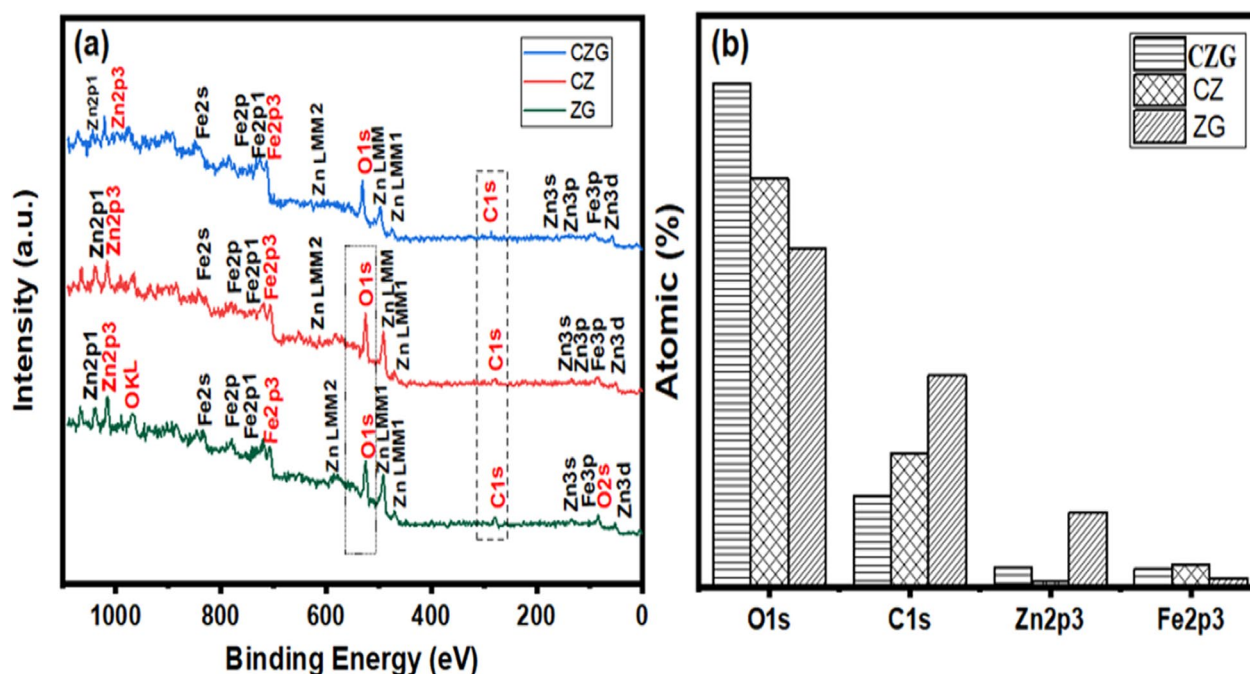


**Fig. 5** a XPS Survey scan of CZG, CZ and ZG b Atomic percentage of various elements

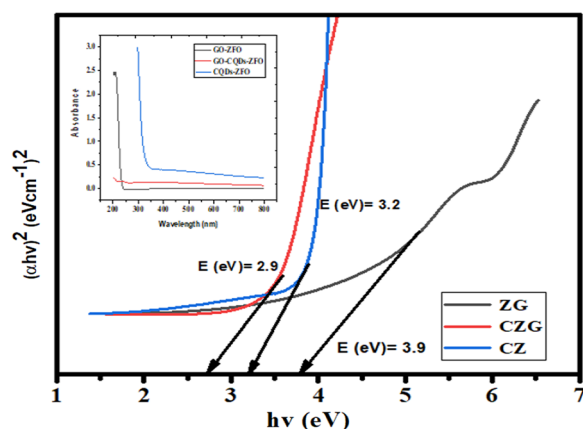


**Fig. 6** Bandgap of binary ZG, CZ, and ternary CZG using Tauc plot

## Optical parameters

### Band gap analysis

The optimization of light requirements is essential for achieving successful photodegradation processes. This optimization is critical for determining the optical characteristics and bandgap of different photocatalysts, as seen in Fig. 6. The energy bandgaps of binary and ternary nanocomposites were calculated using the tauc plot [51]. The investigation focused on the optical absorption properties of the generated samples within the ultraviolet–visible (UV–vis) spectrum, spanning a wavelength range of

300 to 800 nm. Therefore, the findings from XRD and FTIR support the effective synthesis of the ternary nanocomposite. Furthermore, it has been demonstrated by the bandgap analysis that the ternary CZG exhibits a significant degradation due to the efficient separation of electron–hole pairs [35]. The formula used to compute the Tauc plot's bandgap is shown below

$$(\alpha h\nu)^2 = B(h\nu - E_g) \quad (3)$$

The relationship between energy (in eV) and angular velocity ( $h$ ) is given by the equation  $E_g = h\nu$ . The absorption energy is calculated at  $(h)$  value, then projected to  $=0$ . Bandgap energies of 2.7 eV, 3.2 eV, and 3.9 eV were calculated for CZG, CZ, and ZG, respectively. The equation's parameters ( $\alpha$ ,  $B$ , and  $\nu$ ) are the light frequency, the proportionality constant, and the absorption coefficient, respectively. Bandgap values imply that catalysts function in the UV spectrum's ultraviolet light range.

### Point of zero charge

Determining a nanocomposite's point of zero charges (pHpzc) is crucial in assessing its photocatalytic activity. Comprehending the adsorption behavior of dyes is of utmost importance in scientific research. Composite surfaces exhibit a net positive charge when the point of zero charge (pzc) is surpassed by the solution pH.

Conversely, when the pH exceeds the pzc, the composite surfaces acquire a negative charge [52]. The neutral electrical charge of a composite material of magnetic CZG was measured to be 3.33, as shown in Fig. 7. Due to the cationic nature of RhB molecules, a negative charge on the catalyst's surface facilitates adsorption at pH levels higher than the point of zero charge. Therefore, the catalyst surface exhibits a strong electrostatic attraction towards the cationic molecules of the RhB dye, resulting in an enhanced degradation efficiency [53].

### Effect of operational parameters for dye degradation by ternary CZG

#### Effect of pH

The pH of the aqueous solution is a crucial determinant of the photo-efficiency of the photocatalytic system during the photodegradation process. The pH affects the surface charge properties of photocatalysts, including their point of zero charges (pHPZC) and organic molecule adsorption capacity [54]. The study studied the impact of pH on RhB photodegradation by varying pH values from 2 to 9 while maintaining other parameters (catalyst dose: 20 mg/100 mL for CZG ternary, 30 mg/100 mL for binary CZ and ZG, initial dye concentration: 10 ppm, irradiation time: 60 min). The pH of dye solutions was maintained using 0.1 M and 1 mM sodium hydroxide hydrochloric acid solutions. Since Rhodamine B is a cationic dye, it becomes positively charged when dissociated in water. The  $pH_{PZC}$  value for CZG was measured at pH 3.3. Lower pH values than the  $pH_{PZC}$  result in a positively charged catalyst surface, which electrostatically repels positively charged RHB dye molecules. Active spots on the catalyst surface are weak in acidic environments, reducing hydroxyl radical production and dye degradation [55]. According to Fig. 8a, the ternary CZG exhibited 97% photocatalytic degradation in an acidic medium at pH 4 under 60 min

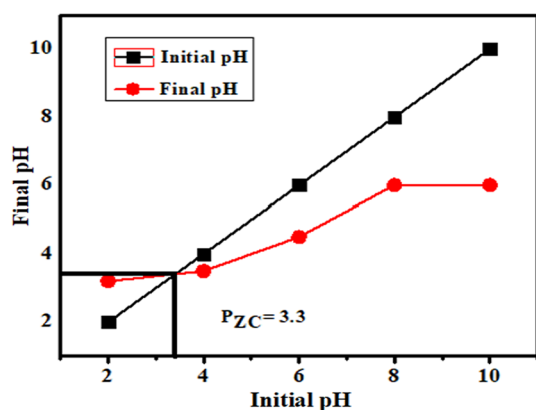


**Fig. 7** Point of zero charge of ternary CZG

of UV-light irradiation. Previously, our research group reported Rhodamine B degradation by iron tungstate-based nanocomposite in the acidic medium at pH 3 owing to the demonstration of a Fenton-like reaction occurring in the dye solution [56]. At an acidic pH, the solution becomes protonated. These protons may then react with superoxide radicals to produce hydroxyl radicals, which will eventually reduce the amount of dye molecules. Similarly, utilizing CQD-based nanocomposites, Malitha and colleagues have proposed that the ideal pH range for RhB and some other cationic dye degradation is 4–6 [57]. Small pH variations may have an impact on the RhB molecule's ability to bind to CQD-based nanocomposite surfaces, changing the adsorption process and photocatalytic oxidation. In another recent study, it was reported that using ferrite-based nanocomposite RhB degradation efficiency was 10–40% in basic medium and enhanced to 99% at pH 3 [42, 58].

Both low and high pH values should result in a net positive charge on the photocatalyst surface. Cationic Rh B dye would bind to the surface of the catalyst more quickly at higher pH levels because the zeta potential decreases with rising pH [58]. Exposing the solution to visible light will excite the electron, resulting in the formation of electron/hole ( $e^-/h^+$ ) pairs. The electron would move from the valence band into the conduction band as a result. The produced holes, either oxidize the Rh B dye immediately, leading to mineralization to  $CO_2$  and  $H_2O$ , or react with OH to produce hydroxyl radical. One possible mechanism by which a low pH value improves photocatalytic degradation is by encouraging the adsorption of Rh B dye onto the photocatalyst outermost layer [58]. Rapid degradation of the dye Rh B occurs at lower pH levels because an increase in the creation of hydroxyl radicals causes them to interact with holes, leading to the production of even more hydroxyl radicals [59, 60]. Rhodamine B is a cationic dye; yet, studies showed that it had no impact on the alkalinity value when the alkalinity level was high enough [61]. Moreover, at alkaline pH values the degradation ability of ternary catalyst was reduced as a result of sludge formation. This sludge was formed because of the reaction of excess hydroxyl radicals and ferrous ions. This sludge blocks the majority active sites of catalyst hence, creating hindrance in charge transfer among the three components [56]. According to Fig. 8a, the ternary CZG exhibited 97% photocatalytic degradation in an acidic medium at pH 4 under 60 min of UV-light irradiation. The ternary CZG at pH 4, binary ZG at pH 5, and CZ at pH 6 degraded 97% 85% and 89% under Ultraviolet light for about the same period suggesting that ternary CZG has improved photocatalytic degradation.

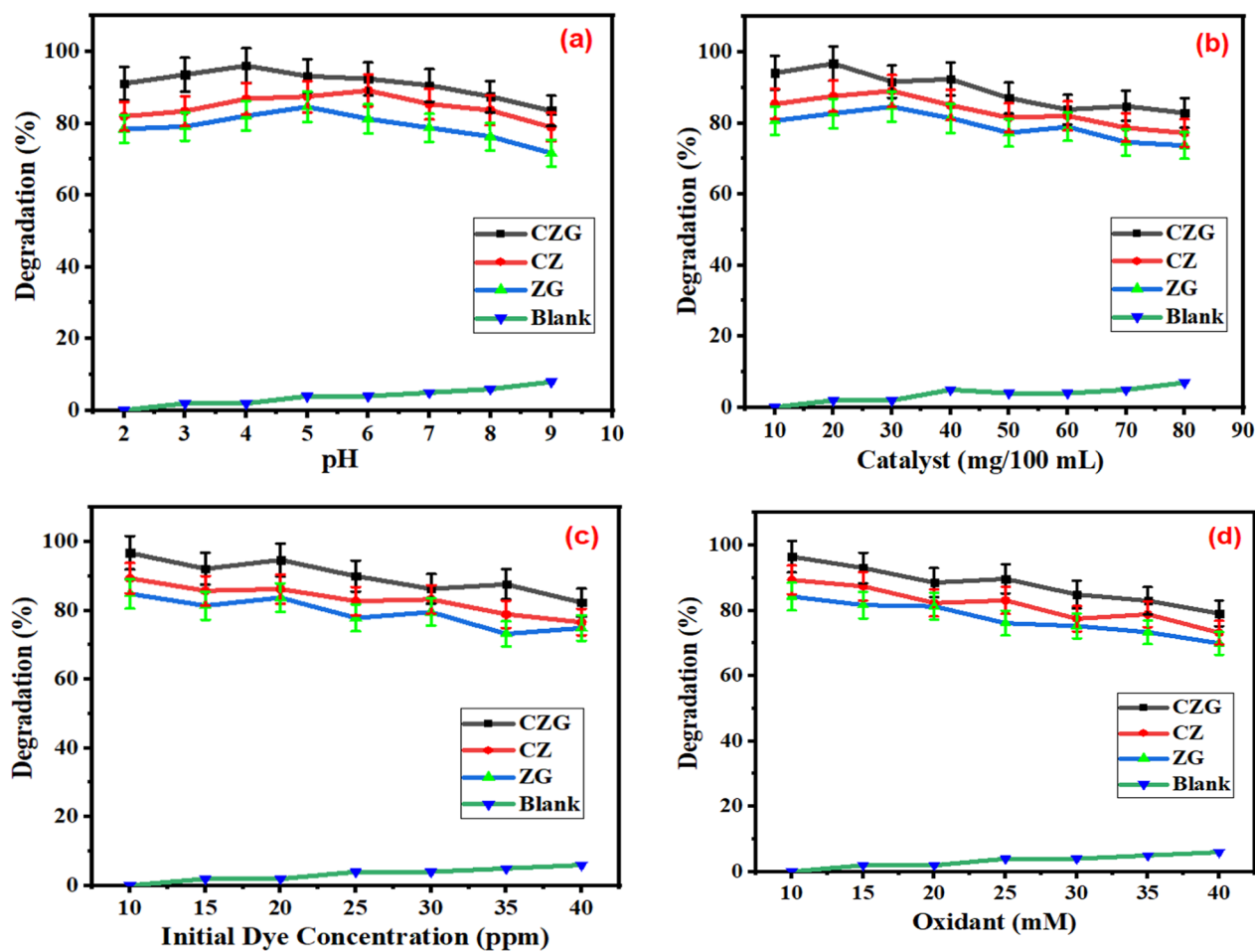


**Fig. 8** Operating parameters **a** pH **b** Catalyst dosage **c** Oxidant dosage **d** Dye Concentration

### Effect of catalyst dose

The quantity of catalyst utilized is crucial for assessing photocatalytic performance and cost. Catalyst loading and photodegradation efficiency were examined for 10 ppm RhB dye solution degradation at 10–80 mg/100 mL, with constant factors (pH=4) for CZG ternary, 5 and 6 pH for binary ZG and CZ, optimum catalyst dose, and 60 min irradiation. Photocatalyst dosages (10 mg–100 mg/L) were studied to determine their impact on degradation. The photodegradation efficiency of CZG increased from 69 to 97% with a catalyst dosage of 10 to 50 mg. The catalyst dosage increases the number of active sites on its surface, leading to increased generation of hydroxyl and superoxide radicals [62]. Reduced light transmission occurs as a result of scattering effects, magnetic nanoparticle formation, and increased suspension turbidity when the dose of the photocatalyst is increased over the threshold [63]. The recommended dose of the photocatalyst is 0.5 g/L, which is determined by several criteria including catalytic efficiency

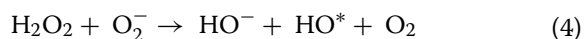
and operating expenditures. Raise the temperature of the Rh B dye bath to improve its oxidation. Elevated electrons move into the conduction band from an optically UV light source. An increase in reactive oxygen species (ROS), or more precisely, the production of extra electron–hole pairs. The RhB dye was oxidized more quickly when used in pairs [64, 65]. The magnetic ternary composites showed improved photodegradation at 20 mg/mL catalyst dosage and 30 mg/100 mL binary ZFO-GO and CQDs- ZFO dose, as seen in Fig. 8b graph. Catalyst doses beyond 20 mg showed a modest rise up to 97% but decreased after 100 mg. Reduced degradation is caused by light interception, preventing photons from reaching adsorbed pollutants, and catalyst aggregation at larger dosages, leading to an absence of active sites [66].

### Effect of oxidant dose

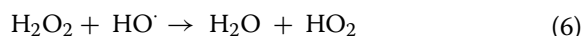
The oxidant dose was adjusted by adjusting hydrogen peroxide from 5 to 40 mM/100 mL in the dye solution after pH, while catalyst concentrations remained

constant. Figure 8c shows a graph produced from experimental data at predefined intervals. Initially, the experiment was done without an oxidant, showing minimal catalyst degradation.

The photocatalytic effectiveness of the catalyst was enhanced when the oxidant concentration grew to a certain degree. Hydroxyl radical ( $\text{OH}\cdot$ ) aids catalysts in decomposing organic dyes more effectively. RhB breakdown often follows the addition of  $\text{H}_2\text{O}_2$ , which captures electrons for hydroxyl radical production [36]. The production of  $\text{OH}\cdot$  radicals accelerates the breakdown of dye RhB by adsorbing it on the catalyst surface. Additional active sites are created upon accepting electrons from the conduction band, generating  $\text{OH}\cdot$ , a crucial dynamic species in degradation [67]. Increasing the oxidant dose to 10 mM/100 mL decreases the photocatalytic activity of CZG. The optimal oxidant dosage for ZFO/GO and CQDs/ZFO was 10 mM/100 mL. Furthermore, hydroxyl radicals contribute to charge separation by removing electrons from the conduction band. Hydroxyl radicals occur when hydrogen peroxide takes an electron from a superoxide radical. Below the optimum threshold,  $\text{H}_2\text{O}_2$  acts as a limiting reagent and the Fenton-like process causes deterioration to occur. When the value is optimized, the photocatalyst activates its active sites, resulting in remarkable deterioration. The efficiency of  $\text{H}_2\text{O}_2$  breakdown decreases as the chance of  $\text{OH}\cdot$  generation increases under acidic environments. Because radical scavenging is reduced, the effectiveness of  $\text{H}_2\text{O}_2$  is enhanced by this delay [68].



After reaching a specific threshold, the photocatalytic efficiency experiences a decline upon further augmentation of the oxidant dosage. This phenomenon can be attributed to the generation of hydrogen peroxide radicals, which exhibit lower reactivity compared to hydroxyl radicals and effectively neutralize them [69].



Therefore, the investigation on degradation revealed that the carbon quantum dots anchored on magnetic graphene oxide exhibited the most optimal photocatalytic efficiency when subjected to an oxidant concentration of 10 mM.

### Effect of initial dye concentration

The concentration of dye adsorbed on the catalyst surface greatly affects dye degradation. The photodegradation of RhB by CZG and other nanocomposites was studied with starting dye concentrations varying from 10 to 40 ppm while maintaining optimal parameters. At low initial RhB load, maximal degradation occurred owing to active site availability and dye molecule-hydroxyl radical reaction on the catalyst surface; enhanced dye concentration leads to saturated active sites on the catalyst surface due to enhanced dye molecule adsorption [70]. The catalyst's surface receives fewer photons, reducing hydroxyl radical production for RhB molecule breakdown [71]. The graph of Fig. 8d shows the performance of all photocatalysts. Maximum degradation occurred for all catalysts at 10 ppm Rhodamine B concentration. The ternary CZG nanocomposite degraded over 97% at increased RhB concentrations. This is because the ternary heterojunction has a larger surface area and can absorb more RhB molecules. After dye molecules degrade on the photocatalyst surface, additional dye molecules quickly occupy the empty active sites [72]. Decreased hydroxyl radical generation due to reduced light intensity at the catalyst surface leads to less effective breakdown of Rhodamine B molecules. The unique ternary magnetic CZG photocatalyst improves RhB degradation even at larger dye loading than conventional photocatalysts.

The dosage of a catalyst determines its limitations for certain organic contaminants in wastewater, which gradually reduces the degradation rate. Graphene oxide-supported composites effectively degrade and avoid agglomeration at increasing concentrations [73].

### Effect of irradiation time

Photocatalytic reactions necessitate the utilization of light energy, making light illumination conditions a critical factor influencing the performance of photocatalysts. The presented data illustrates the decomposition efficiency of Rhodamine B in comparison to CZG, CZ, and ZG under ultraviolet irradiation. The dye solutions underwent light irradiation for approximately one hour under ideal conditions for each catalyst. The modified Rhodamine B solutions' ultraviolet-visible absorption spectra were obtained after 10 min of UV-irradiation in the 250–400 nm wavelength range.

The alterations in the dye solution's spectral properties were observed by constructing a graph depicting the absorbance values as a function of time. The degradation trend increases over time, as illustrated in Figure 9a. The dye colour exhibited a noticeable decrease in intensity after 30 min of irradiation in the case of the newly developed magnetic CZG. Furthermore, the dye

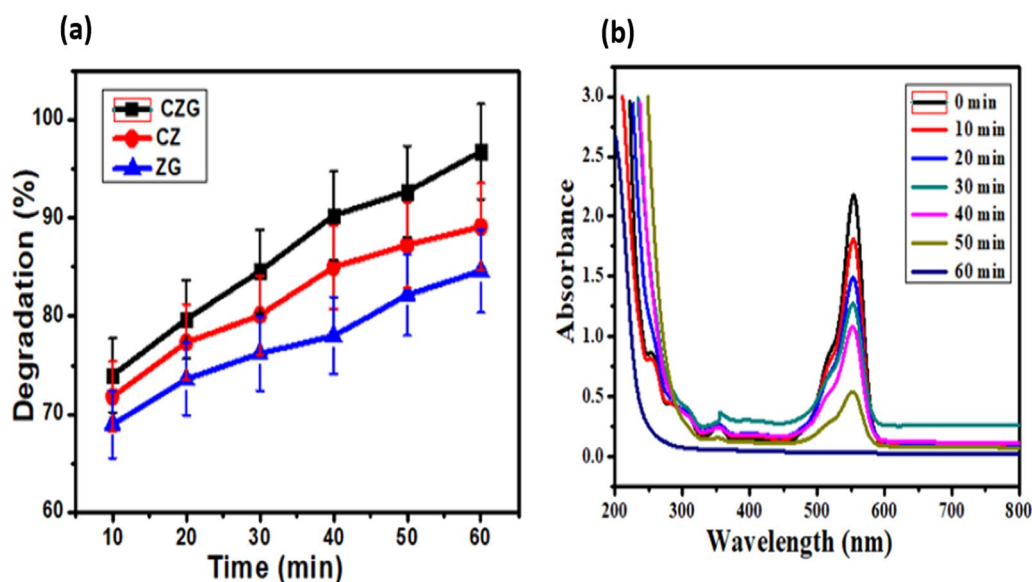


**Fig. 9** a Time parameter b UV-vis spectral scan of RhB degradation with time

completely degraded within approximately 60 min under the same conditions. In contrast, the dye intensity gradually decreased for the ternary CZF and binary ZG and CZ samples. Light irradiation induces a rapid decrease in absorbance, which signifies the progressive degradation of chromophore groups accountable for the manifestation of colour Fig. 9a. In addition, the data is subjected to the application of kinetic models.

The ultraviolet-visible scan of the RhB dye over time Fig. 9b demonstrates the deterioration of the RhB dye over time when exposed to novel magnetic CZG nanocomposites. The UV-Vis absorption spectra indicate that magnetic CZG exhibited enhanced rhodamine B (RhB) removal.

### Reaction kinetics

The degradation of rhodamine B was investigated by fitting first and second-order kinetic models to available experimental data. The equations representing these models are listed below [73]. The graph demonstrates that the natural logarithm of the beginning concentration divided by the concentration at time  $t$ , denoted as “ $\ln C_0 / C_t$ ,” exhibits a linear relationship with the variable  $t$ . The rate constant of a first-order reaction may be computed by determining the slope of the corresponding graph. The rate constant  $K_2$  associated with a second-order reaction, like  $K_1$ , is proportional to the slope of the relationship between “ $1 / C_t - 1 / C_0$ ” and time. The table includes rate constants and their associated  $R^2$  values. The first-order kinetics matches the photocatalytic degradation process most compared to pseudo-one-order and

second-order models. This is because a higher value was discovered for  $R^2$ .

$$\ln C_t = K_1 t (\text{Pseudo First order}) \quad (8)$$

$$\ln C_0 / C_t = K_2 t (\text{First order}) \quad (9)$$

$$1/C_t - 1/C_0 = K_3 t (\text{Second order}) \quad (10)$$

“ $C_0$ ” denotes the concentration of the dye solution at the start of time, and “ $C_t$ ” represents the concentration at the moment represented by “ $t$ .” [74]. Reaction rate constants are indicated by the letters “ $K$ ”: “ $K_1$ ” for pseudo-first-order reactions, “ $K_2$ ” for first-order responses, and “ $K_3$ ” for second-order processes.

As shown in Fig. 10, the time required to complete a reaction is directly proportional to the natural logarithm of the ratio of the initial concentrations ( $\ln(C_0/C_t)$ ). This result is consistent with first-order kinetics for RhB photodegradation by ternary nanocomposites. The apparent first-order rate constant, given by the symbol  $k$ , corresponds to the slope of the line depicting the concentration of  $C_0/C_t$  as a function of time, as shown by linear regression analysis. When considering the first-order process, the rate constants  $k_2$  are more effective than  $K_1$  and  $K_3$  when UV light is present.

### Reusability analysis and iron leaching

Under the optimal pH, catalyst dosage, oxidant concentration, dye concentration, and irradiation duration, the stability and reusability of the catalysts for CZG were

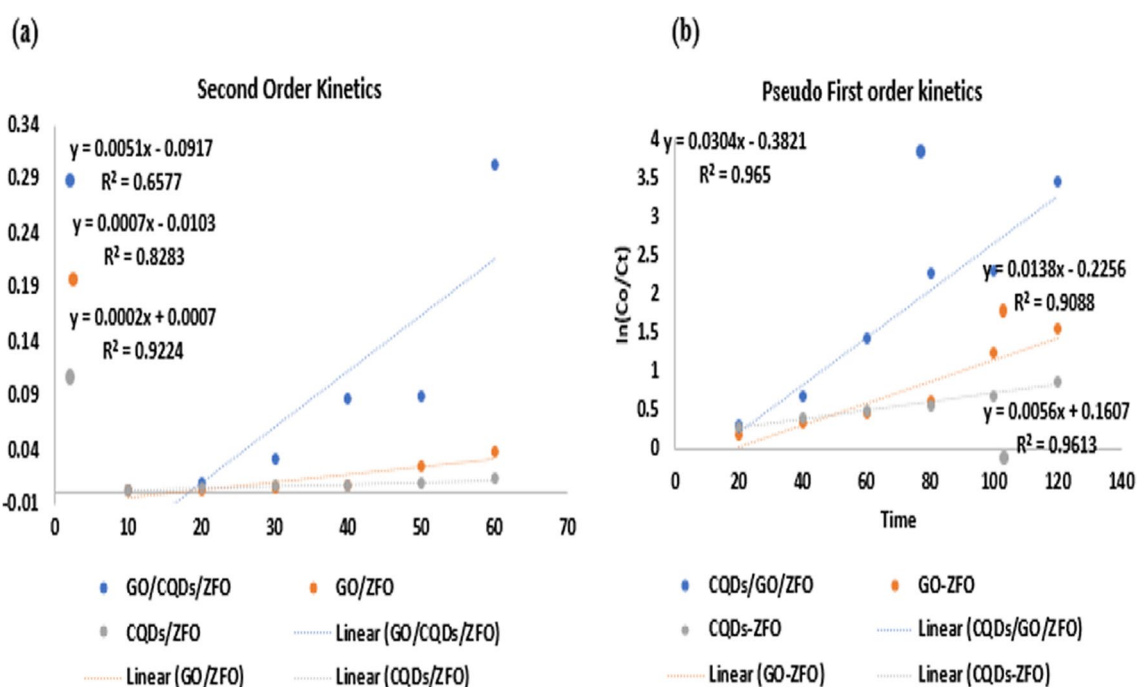


**Fig. 10** Reaction kinetic (a) second order (b) Pseudo First order

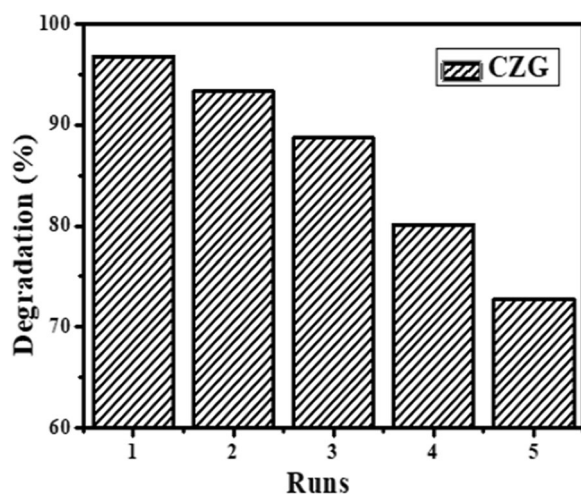


**Fig. 11** Reusability study by ternary CZF nanocomposite

studied. Magnets on the outside helped get the catalysts out so they could be reused. Catalysts were washed, dried in an oven, reweighed, and reused after being extracted from reaction solutions. Degradation efficiency was shown to drop from 95 to 68% after the 5th cycle (Fig. 11).

Heterogeneous photocatalysts must be stable enough for wastewater treatment without allowing metals to leach from the solid into the liquid. Atomic absorption

spectroscopy measurements of iron leaching were taken after each experiment to evaluate catalyst stability. The catalyst is stable and may be reused several times without significantly degrading its photocatalytic efficacy if the concentration of iron and zinc leaching (0.19 and 0.26 mg/L) is less than 0.32 mg/L. The measured iron leaching was less than a tenth of the European Union limit (2.0 mg/L) [50]. However, even this slow and steady metal release may render the catalysts ineffective. After repeated usage, the active sites on the catalyst's surface may get blocked or diminished, leading to a decline in photocatalytic effectiveness. The catalysts' structure and performance may be affected by several factors [46].

#### Toxicity analysis

The Primary and secondary treated wastewater is used for horticulture, landscape irrigation, and food crop irrigation. Advanced oxidation techniques decompose organic contaminants into carbon dioxide during tertiary wastewater treatment. Therefore, the water may replace surface groundwater. Due to environmental and socio-economic considerations, treated wastewater and ultraviolet light nanocomposites are used to grow food crops [75]. Under UV light, magnetic nanocomposites must be tested for pollutant degradation in dye-loaded wastewater treatment. The byproducts' qualities determine the outcome. To accomplish our goal, we used water treated with Rhodamine B and carbon quantum dots anchored

on magnetic graphene oxide on highly sensitive wheat seedlings. A 10-mL solution of treated RhB dye was used to immerse filter sheets and seeds, which were then covered with glass lids [76]. The Petri plates were incubated at ambient temperature for 24 h. As seen in Fig. 7, wheat seedlings germinated within two days. The seeds did not blacken in RhB-treated wastewater. This shows that the treated water by novel photocatalyst, is safe for agricultural irrigation. Thus, treated water may be used for irrigation under optimal circumstances [23]. Figure 12 shows wheat seed germination by treated dye water by ternary CZG nanocomposite.

#### Radical scavenging experiment

Photocatalytic degradation involves the participation of reactive species, including  $h^+$ ,  $e^-$ , and hydroxyl radicals. The use of radical scavenging species may accomplish the assessment of the efficacy of radicals involved in degradation processes. Various radical scavengers were used in this study, including Ethylene diamine tetraacetate (EDTA) for hole scavenging, Potassium dichromate ( $K_2Cr_2O_7$ ) for electron scavenging, ascorbic acid for superoxide radical scavenging, and Dimethyl sulfoxide (DMSO) for OH radical scavenging. A concentration of 5 mM (mM) was used for each scavenger, and the experiment was conducted under ultraviolet (UV) light under the most favorable circumstances. The findings indicate that adding DMSO significantly mitigated the deterioration of the dye solution. The use of DMSO in the GO/ZFO/CQDs system decreased degradation from an initial value of 85% to a final value of 29%. Likewise, the presence of electron and hole scavengers reduced degradation (Fig. 13).

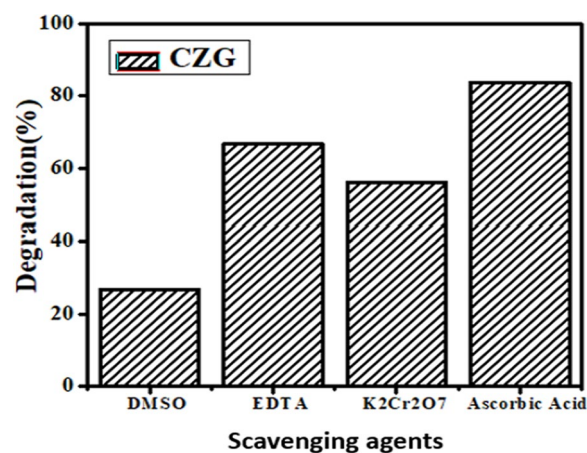


Fig. 13 Scavenging study by ternary CZG

#### Proposed mechanism

The proposed mechanism for dye photodegradation is based on holes and hydroxyl radicals, both of which play significant roles in the process. Absorption of light energy over the bandgap energy, according to current understanding, results in the production of holes and electrons, which assist in the deterioration process. The breakdown process is sparked by reactive oxygen species, of which electrons and holes are examples. Carbon quantum dots anchored on magnetic graphene oxide improve charge transfer, decreasing the bandgap of zinc ferrite. As a result, UV light rapidly excites electrons in the valence band of ZnFe, causing them to move into the conduction band (CB). While the positively charged  $h^+$  atoms stay in the valence band, photoexcited electrons go from the VB of zinc ferrite to the CB of Carbon quantum dots. The recombination process is prolonged because

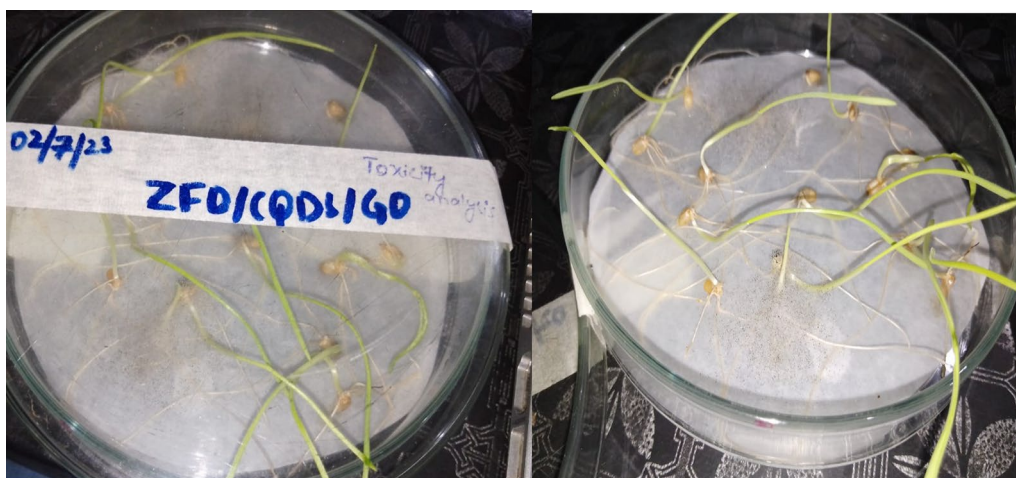
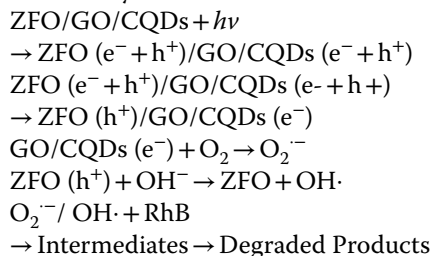


Fig. 12 Assessment of Toxicity analysis of treated RhB water by ternary CZG over wheat seed

graphene oxide induces the oxide holes to go nearer the valence band (VB) of ZFO. Photogenerated holes acted onto the  $\text{H}_2\text{O}_2$ , causing it to undergo reduction, producing a superoxide radical. Graphene oxide acts as a sinking medium. Therefore, electrons and holes recombine slowly. The following process may explain this. Figure 14 shows the proposed mechanism of RhB degradation by novel ternary CZG.



### Response surface methodology (RSM)

The response surface approach has been proven to be an effective tool for optimizing a wide range of photocatalytic degradation process variables. This work investigated methylene blue's degradation rate by manipulating many variables using the central composite design (CCD) method. To maximize degradation, as measured by the response variable, we used central composite design

to regulate and manipulate many relevant factors. This included pH, catalyst dosage, and oxidant dose.

### Analysis of variance (ANOVA)

The selected model strongly affects the optimized variables, as the fit summary graphic shows. The model's strong  $R^2$  value reveals its impressive predictive power. Using a quadratic model, it is found that numerous variables—pH, catalyst concentration, and oxidant—significantly correlated with observed degradation as shown in Table 1. Mathematical modeling in a second-order polynomial equation was utilized to investigate the connection between the abovementioned factors and the rate at which rhodamine B dye degrades. This equation may also be written as:

$$Y = \beta_0 + \sum_{i=1}^k \beta_i x_i + \sum_{i=1}^k \beta_{ii} x_i^2 + \sum_{i=1}^k \sum_{i \neq j=1}^k \beta_{ij} x_i x_j + \epsilon \quad (11)$$

Lack of fit and regression analysis helps determine whether a model is suitable for a given dataset. The p-value tells you how significant a certain variable is statistically. A model is deemed insignificant if its p-value is more than 0.1000, whereas a p-value of less than 0.05 suggests statistical significance. The statistical model

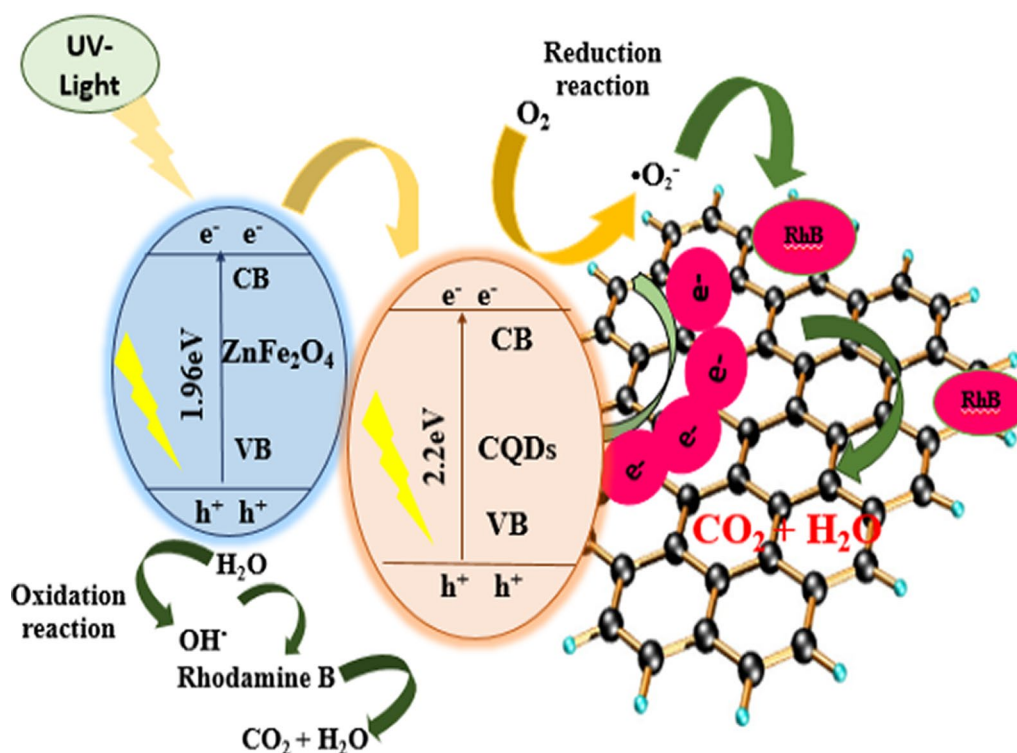


**Fig. 14** Proposed mechanism of Dye RhB degradation using ternary CZG

**Table 1** ANOVA table for RhB degradation by ternary CZG

Source	Sum of square	Df	F-value	P-value	
Model	12,553.35	9	1394.82	<0.0001	Significant
A-pH	2345.77	1	2345.77	<0.0001	
B-Catalyst Dose	21.80	1	28.10	0.4038	
C-Oxidant dose	67.10	1	67.10	0.5171	
AB	167.53	1	167.53	0.0362	
AC	143.74	1	143.74	0.0491	
BC	133.39	1	13.39	0.5099	
A <sup>2</sup>	6052.57	1	6052.57	<0.0001	
B <sup>2</sup>	2595.85	1	2595.85	<0.0001	
C <sup>2</sup>	2949.02	1	2949.02	<0.0001	
Residual	286.78	10	28.68		
Lack of fit	286.78	5	57.36		Non-significant
Pure error	0.0000	5	0.0000		
Cor total	12,840.13	19			
Std. Dev	5.36		R <sup>2</sup>	0.9777	
Mean	64.08		Adjusted R <sup>2</sup>	0.9576	
C.V.%	8.36		Predicted R <sup>2</sup>	0.8311	
Press			Adeq Precision	21.1282	

is considered significant when the p-value is less than 0.0001.

The percentage decline is the dependent variable here, and Y is the reaction. The variable to which the coefficient  $\beta^{\circ}$  is assigned and its associated value are both known. Linearity coefficients are denoted by  $\beta_i$ , and those of quadraticity by  $\beta_{ii}$ . The coefficient  $\beta_{ij}$  represents the interplay between two variables. In addition,  $x \beta_i$  and  $x \beta_j$  signify the encoded values for the independent variables, whereas the symbol denotes random errors

$$\begin{aligned}
 Y = & 97.00 + 13.11 * A + 1.26 * B + 2.22 * C \\
 & - 4.58 * AB - 4.24 * AC + 1.29 * BC - 20.49 \\
 & * A^2 + -13.42 * B^2 - 14.30 * C^2
 \end{aligned}
 \tag{12}$$

Y is the proportion of rhodamine B dye that has been destroyed, whereas A, B, and C are the pH, catalyst concentration, and oxidant dosage, respectively. The variables AB, AC, and BC show the linear influence, whereas the quadratic effect is demonstrated by the variables A<sup>2</sup>, B<sup>2</sup>, and C<sup>2</sup>.

A contour plot and a three-dimensional display illustrate the relationship between the two variables. The experiment was conducted at a catalyst concentration of 10–30 mg per 100 mL and a pH range of 2–6. The degradation rate rises when the pH varies from 2 to 9, peaking at a pH of 4 before declining at higher pH values. In a concentration range of 10–20 mg/100 mL, photocatalysis showed improved performance in the degradation of rhodamine B. Increased surface area of the photocatalyst

allows for more sites for dye adsorption, which may explain the observed improvement. Nanoparticle aggregation, which leads to active site obstruction, becomes more evident when catalyst concentration is raised. Consequently, having a photocatalyst present slows down the pace at which an object degrades when exposed to UV radiation.

The oxidants were used at dosages ranging from 5 to 15 mM. Photocatalytic activity increased when the oxidant concentration was increased to 10 mM. The experiments lasted 60 min and used catalyst concentrations ranging from 10 to 20 mg/100 mL. The degradation rate was greatest at a concentration of 20 mg per 100 mL for 60 min. Figure 15 depicts a graphical representation of their mutual interaction.

## Conclusion

The dye rhodamine B breakdown process under UV light is significantly aided by the nanocomposite CZG, which possesses unique features. Hydrothermal synthesis was used to synthesize the ternary carbon quantum dots anchored on magnetic graphene oxide. When exposed to UV light, the composite efficiently degrades the rhodamine B dye. Degradation efficiencies of binary and ternary nanocomposites were also compared, which motivated the synthesis of ZG and CZ. Clearance efficiency for RhB dye was as high as 97% after an hour after being exposed to CZG. Characterization techniques such as scanning electron microscopy with energy-dispersive X-ray spectroscopy, Fourier-transform infrared

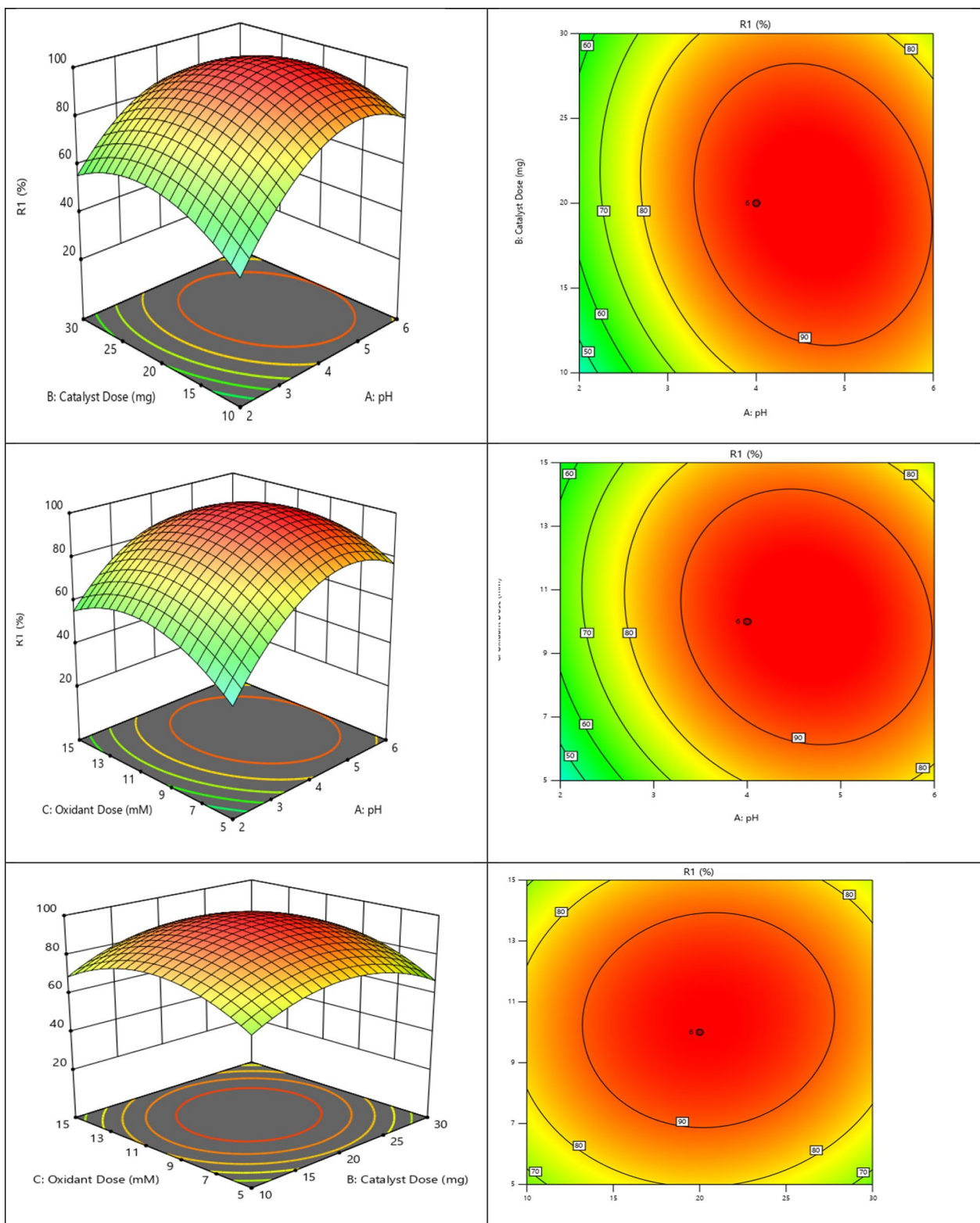


Fig. 15 Contour and 3D graphs of CZG

spectroscopy, X-ray diffraction, and ultraviolet–visible diffuse reflectance spectroscopy were used to evaluate the shape and crystal structure of the newly developed nano-hybrid. This work formed a heterojunction between ZFO, CQDs, and GO, contributing to increased photocatalytic efficiency. There was little catalyst loss and effective deterioration up to the fifth cycle in a series of five cycles used to assess the photostability of the photocatalyst.

#### Acknowledgements

The authors extend their appreciation to the Researchers Supporting Project number (RSP2025R381), King Saud University, Riyadh, Saudi Arabia.

#### Author contributions

W.Q. and N.T. involved in investigation, data curation, methodology and Original draft preparation, M.Z. contributed in supervision, conceptualization, project administration, writing—review and editing., S.N. and M.Y. contributed in software, formal analysis and data curation, A.A. managed the resources and visualization, Q. A. validation and methodology, G.M. investigation, conceptualization, writing—review and editing and all authors reviewed the manuscript.

#### Funding

The authors extend their appreciation to the Researchers Supporting Project number (RSP2025R381), King Saud University, Riyadh, Saudi Arabia.

#### Availability of data and materials

The data generated or analyzed during this study are included in this manuscript.

#### Declarations

#### Ethics approval and consent to participate

Not applicable.

#### Consent for publication

Not applicable.

#### Competing interests

The authors declare no competing interests.

Received: 3 March 2024 Accepted: 21 March 2025

Published online: 02 April 2025

#### References

- Pala EM. Ultrastructural deformities in the scales of *Cyprinus carpio* inhabiting two government-sponsored fish farms in north-east India contaminated by municipal wastes and other pollutants. *Microsc Microanal.* 2018;24(6):729–33.
- Naushad M, Sharma G, Alotman ZA. Photodegradation of toxic dye using Gum Arabic-crosslinked-poly (acrylamide)/Ni (OH) 2/FeOOH nanocomposites hydrogel. *J Clean Prod.* 2019;241: 118263.
- Alosaimi EH, et al. Investigation of Fe-doped graphitic carbon nitride-silver tungstate as a ternary visible light active photocatalyst. *J Chem.* 2021;2021:1–18.
- Tatarchuk T, et al. Adsorptive removal of toxic Methylene Blue and Acid Orange 7 dyes from aqueous medium using cobalt-zinc ferrite nano-adsorbents. *Desalin Water Treat.* 2019;150:374–85.
- Pandis PK, et al. Key points of advanced oxidation processes (AOPs) for wastewater, organic pollutants and pharmaceutical waste treatment: a mini review. *ChemEngineering.* 2022;6(1):8.
- Pesqueira JF, Pereira MFR, Silva AM. A life cycle assessment of solar-based treatments (H<sub>2</sub>O<sub>2</sub>, TiO<sub>2</sub> photocatalysis, circumneutral photo-Fenton) for the removal of organic micropollutants. *Sci Total Environ.* 2021;761: 143258.
- Espulgas S, et al. Comparison of different advanced oxidation processes for phenol degradation. *Water Res.* 2002;36(4):1034–42.
- Tang J, Wang J. Metal organic framework with coordinatively unsaturated sites as efficient Fenton-like catalyst for enhanced degradation of sulfamethazine. *Environ Sci Technol.* 2018;52(9):5367–77.
- Khaki MRD, et al. Application of doped photocatalysts for organic pollutant degradation—a review. *J Environ Manage.* 2017;198:78–94.
- Kasiri M, Aleboye H, Aleboye A. Degradation of Acid Blue 74 using Fe-ZSM5 zeolite as a heterogeneous photo-Fenton catalyst. *Appl Catal B.* 2008;84(1–2):9–15.
- Oladipo AA, Ifebajo AO, Gazi M. Magnetic LDH-based CoO–NiFe<sub>2</sub>O<sub>4</sub> catalyst with enhanced performance and recyclability for efficient decolorization of azo dye via Fenton-like reactions. *Appl Catal B.* 2019;243:243–52.
- Li Y, et al. Enhanced visible light assisted Fenton-like degradation of dye via metal-doped zinc ferrite nanosphere prepared from metal-rich industrial wastewater. *J Taiwan Inst Chem Eng.* 2019;96:185–92.
- Ansari H, Oladipo AA, Gazi M. Alginate-based porous polyHIPE for removal of single and multi-dye mixtures: competitive isotherm and molecular docking studies. *Int J Biol Macromol.* 2023;246: 125736.
- Liu W, et al. Treatment of Cr(VI)-containing Mg(OH)<sub>2</sub> nanowaste. *Angew Chem Int Ed.* 2008;47(30):5619–22.
- Mao M, et al. Selective capacitive recovery of rare-earth ions from wastewater over phosphorus-modified TiO<sub>2</sub> cathodes via an electro-adsorption process. *Environ Sci Technol.* 2024;58(31):14013–21.
- Liu W, et al. Effective extraction of Cr(VI) from hazardous gypsum sludge via controlling the phase transformation and chromium species. *Environ Sci Technol.* 2018;52(22):13336–42.
- Wang Y, et al. Efficient removal of dibutyl phthalate from aqueous solutions: recent advances in adsorption and oxidation approaches. *Reaction Chem Eng.* 2024;9(6):1276–91.
- Qiu X, et al. Applications of nanomaterials in asymmetric photocatalysis: recent progress, challenges, and opportunities. *Adv Mater.* 2021;33(6):2001731.
- Rafique M, et al. Plant-mediated green synthesis of zinc oxide nanoparticles from *Syzygium Cumini* for seed germination and wastewater purification. *Int J Environ Anal Chem.* 2022;102(1):23–38.
- Zhang K, et al. Novel method of constructing CdS/ZnS heterojunction for high performance and stable photocatalytic activity. *J Photochem Photobiol, A.* 2019;380: 111859.
- Jasrotia R, et al. Photocatalytic application of magnesium spinel ferrite in wastewater remediation: a review. *J Magn Alloys.* 2024.
- Arimi A, et al. Visible-light photocatalytic activity of zinc ferrites. *J Photochem Photobiol, A.* 2018;366:118–26.
- Khan M, et al. Visible light assisted photocatalytic degradation of methylene blue using iodine doped Fe<sub>3</sub>O<sub>4</sub>-GO composite. *Optik.* 2023;290: 171282.
- Chen Y, et al. Magnetic recyclable lanthanum-nitrogen co-doped titania/strontium ferrite/diatomite heterojunction composite for enhanced visible-light-driven photocatalytic activity and recyclability. *Chem Eng J.* 2019;373:192–202.
- Lim SY, Shen W, Gao Z. Carbon quantum dots and their applications. *Chem Soc Rev.* 2015;44(1):362–81.
- Jiang R, et al. Fabrication of Fe<sub>3</sub>O<sub>4</sub> quantum dots modified BiOCl/BiVO<sub>4</sub> pn heterojunction to enhance photocatalytic activity for removing broad-spectrum antibiotics under visible light. *J Taiwan Inst Chem Eng.* 2019;96:681–90.
- Manikandan V, Lee NY. Green synthesis of carbon quantum dots and their environmental applications. *Environ Res.* 2022;212: 113283.
- Das R, Bandyopadhyay R, Pramanik P. Carbon quantum dots from natural resource: a review. *Mater Today Chem.* 2018;8:96–109.
- de Oliveira BP, da Silva Abreu FOM. Carbon quantum dots synthesis from waste and by-products: perspectives and challenges. *Mater Lett.* 2021;282:128764.
- Rather RA, Lo IM. Photoelectrochemical sewage treatment by a multi-functional g-C<sub>3</sub>N<sub>4</sub>/Ag/AgCl/BiVO<sub>4</sub> photoanode for the simultaneous degradation of emerging pollutants and hydrogen production, and the disinfection of *E. coli*. *Water Res.* 2020;168:115166.

31. Margha FH, et al. Bi<sub>2</sub>O<sub>3</sub>–BiFeO<sub>3</sub> glass-ceramic: controllable β-/γ-Bi<sub>2</sub>O<sub>3</sub> transformation and application as magnetic solar-driven photocatalyst for water decontamination. *ACS Omega*. 2020;5(24):14625–34.
32. Niu J, et al. Facile synthesis of γ-Fe<sub>2</sub>O<sub>3</sub>/BiOI microflowers with enhanced visible light photocatalytic activity. *Mater Des*. 2018;150:29–39.
33. Xia D, et al. Enhanced performance and conversion pathway for catalytic ozonation of methyl mercaptan on single-atom Ag deposited three-dimensional ordered mesoporous MnO<sub>2</sub>. *Environ Sci Technol*. 2018;52(22):13399–409.
34. Guo W, et al. Morphology-controlled preparation and plasmon-enhanced photocatalytic activity of Pt–BiOBr heterostructures. *J Hazard Mater*. 2016;308:374–85.
35. Sun L, et al. Antibacterial activity of graphene oxide/g-C<sub>3</sub>N<sub>4</sub> composite through photocatalytic disinfection under visible light. *ACS Sustain Chem Eng*. 2017;5(10):8693–701.
36. Tahir N, et al. Ternary silver tungstate–MoS<sub>2</sub>/graphene oxide heterostructure nanocomposite for enhanced photocatalysis under visible light and antibacterial activity. *J Photochem Photobiol, A*. 2023;436:114376.
37. Elgorban AM, Al Kheraif AA, Syed A. Construction of Ag<sub>2</sub>WO<sub>4</sub> decorated CoWO<sub>4</sub> nano-heterojunction with recombination delay for enhanced visible light photocatalytic performance and its antibacterial applications. *Colloids Surfaces A Physicochem Eng Aspects*. 2021;629:127416.
38. Surekha G, et al. FTIR, Raman and XRD analysis of graphene oxide films prepared by modified Hummers method. in *Journal of Physics: Conference Series*. 2020. IOP Publishing.
39. Zhang L, et al. Corn cob residues as carbon quantum dots sources and their application in detection of metal ions. *Ind Crops Prod*. 2019;133:18–25.
40. Nadeem N, et al. Improved photocatalytic degradation of dye using coal fly ash-based zinc ferrite (CFA/ZnFe<sub>2</sub>O<sub>4</sub>) composite. *Int J Environ Sci Technol*. 2021; p. 1–16.
41. Baynosa ML, et al. Eco-friendly synthesis of recyclable mesoporous zinc ferrite@ reduced graphene oxide nanocomposite for efficient photocatalytic dye degradation under solar radiation. *J Colloid Interface Sci*. 2020;561:459–69.
42. Zaman F, et al. Enhanced photocatalytic degradation of organic dyes by carbon quantum dots–ZnFe<sub>2</sub>O<sub>4</sub> composites. *J Alloys Compounds*. 2024;983:173860.
43. Masud J, et al. Copper selenides as high-efficiency electrocatalysts for oxygen evolution reaction. *ACS Appl Energy Mater*. 2018;1(8):4075–83.
44. Jia J, et al. Orange-emitting N-doped carbon dots as fluorescent and colorimetric dual-mode probes for nitrite detection and cellular imaging. *J Mater Chem B*. 2020;8(10):2123–7.
45. Ahmadpour N, et al. Photocatalytic degradation of model pharmaceutical pollutant by novel magnetic TiO<sub>2</sub>@ ZnFe<sub>2</sub>O<sub>4</sub>/Pd nanocomposite with enhanced photocatalytic activity and stability under solar light irradiation. *J Environ Manage*. 2020;271: 110964.
46. Nadeem N, et al. Degradation of reactive dye using heterogeneous photo-Fenton catalysts: ZnFe<sub>2</sub>O<sub>4</sub> and GO–ZnFe<sub>2</sub>O<sub>4</sub> composite. *Mater Res Express*. 2020;7(1): 015519.
47. Ahmed HM, et al. Preparation of carbon quantum dots/polyaniline nanocomposite: towards highly sensitive detection of picric acid. *Spectrochim Acta Part A Mol Biomol Spectrosc*. 2021;260: 119967.
48. Jamila GS, et al. Nitrogen doped carbon quantum dots and GO modified WO<sub>3</sub> nanosheets combination as an effective visible photo catalyst. *J Hazard Mater*. 2020;382: 121087.
49. Hammouche J, et al. Enhanced photocatalytic performance of zinc ferrite nanocomposites for degrading methylene blue: effect of nickel doping concentration. *J Inorg Organomet Polym Mater*. 2021;31:3496–504.
50. Tahir N, et al. Impact of alternate Mn doping in ternary nanocomposites on their structural, optical and antimicrobial properties: Comparative analysis of photocatalytic degradation and antibacterial activity. *J Environ Manage*. 2023;337: 117706.
51. Sudhaik A, et al. Peroxymonosulphate-mediated metal-free pesticide photodegradation and bacterial disinfection using well-dispersed graphene oxide supported phosphorus-doped graphitic carbon nitride. *Appl Nanosci*. 2020;10:4115–37.
52. Luciano AJR, et al. Manganese ferrite dispersed over graphene sand composite for methylene blue photocatalytic degradation. *J Environ Chem Eng*. 2020;8(5): 104191.
53. Penke YK, et al. Al<sup>3+</sup>-doped 3d-transitional metal (Mn/Cu) ferrite impregnated rGO for PEC water-splitting/supercapacitor electrode with oxygen vacancies and surface intercalation aspects. *Compos B Eng*. 2020;202: 108431.
54. Ahmadi S, et al. Praseodymium-doped cadmium tungstate (CdWO<sub>4</sub>) nanoparticles for dye degradation with sonocatalytic process. *Polyhedron*. 2020;190: 114792.
55. Nie M, et al. Degradation of chloramphenicol by thermally activated persulfate in aqueous solution. *Chem Eng J*. 2014;246:373–82.
56. Irfan M, et al. Enhanced photo-Fenton degradation of Rhodamine B using iodine-doped iron tungstate nanocomposite under sunlight. *Int J Environ Sci Technol*. 2023;20(4):3645–60.
57. Malitha MD, et al. Fabrication of a reusable carbon quantum dots (CQDs) modified nanocomposite with enhanced visible light photocatalytic activity. *Sci Rep*. 2024;14(1):17976.
58. Jasim NA, Ebrahim SE, Ammar SH. Photocatalytic degradation of Rhodamine B using CoxZn1-xFe<sub>2</sub>O<sub>4</sub> nanocomposite under visible light irradiation: synthesis, characterization and its application. *Alex Eng J*. 2023;82:557–76.
59. Fareghi-Alamdari R, Zandi F, Keshavarz MH. Copper–cobalt synergy in Cu<sub>1-x</sub>Co<sub>x</sub>Fe<sub>2</sub>O<sub>4</sub> spinel ferrite as a highly efficient and regioselective nanocatalyst for the synthesis of 2, 4-dinitrotoluene. *RSC Adv*. 2015;5(88):71911–21.
60. Ebrahim SE. Removal of fluoride ions from wastewater using green and blue-green algae biomass in a fluidized bed system. *J Eng*. 2016;22(2):111–27.
61. Mafossa AB, et al. Removal of organic dyes from water and wastewater using magnetic ferrite-based titanium oxide and zinc oxide nanocomposites: a review. *Catalysts*. 2021;11(12):1543.
62. Oladipo AA. Cu<sub>0</sub>-doped graphitic carbon quantum dots for rapid electrochemical sensing of glyphosate herbicide in environmental samples. *Microchem J*. 2024;200: 110294.
63. Nandan R, Gautam A, Nanda KK. Anthocephalus cadamba shaped FeNi encapsulated carbon nanostructures for metal–air batteries as a resilient bifunctional oxygen electrocatalyst. *J Mater Chem A*. 2018;6(41):20411–20.
64. Bayantong ARB, et al. Adsorptive removal of dye in wastewater by metal ferrite-enabled graphene oxide nanocomposites. *Chemosphere*. 2021;274: 129518.
65. Farhan RZ, Ebrahim SE. Preparing nanosilica particles from rice husk using precipitation method. *Baghdad Sci J*. 2021;18(3):0494–0494.
66. Hu K, et al. Ternary Z-scheme heterojunction of Bi<sub>2</sub>WO<sub>6</sub> with reduced graphene oxide (rGO) and meso-tetra (4-carboxyphenyl) porphyrin (TCPP) for enhanced visible-light photocatalysis. *J Colloid Interface Sci*. 2019;540:115–25.
67. Chu W, Choy W, So T. The effect of solution pH and peroxide in the TiO<sub>2</sub>-induced photocatalysis of chlorinated aniline. *J Hazard Mater*. 2007;141(1):86–91.
68. Han Y-F, et al. Preparation of nanosized Mn<sub>3</sub>O<sub>4</sub>/SBA-15 catalyst for complete oxidation of low concentration EtOH in aqueous solution with H<sub>2</sub>O<sub>2</sub>. *Appl Catal B*. 2007;76(3–4):227–34.
69. Visa M, Bogatu C, Duta A. Tungsten oxide–fly ash oxide composites in adsorption and photocatalysis. *J Hazard Mater*. 2015;289:244–56.
70. Oladipo AA, Mustafa FS. Bismuth-based nanostructured photocatalysts for the remediation of antibiotics and organic dyes. *Beilstein J Nanotechnol*. 2023;14(1):291–321.
71. Nawaz A, et al. Fabrication and characterization of new ternary ferrites-chitosan nanocomposite for solar-light driven photocatalytic degradation of a model textile dye. *Environ Technol Innov*. 2020;20: 101079.
72. Mushtaq F, et al. MnFe<sub>2</sub>O<sub>4</sub>/coal fly ash nanocomposite: a novel sunlight-active magnetic photocatalyst for dye degradation. *Int J Environ Sci Technol*. 2020;17:4233–48.
73. Tabasum A, et al. UV-accelerated photocatalytic degradation of pesticide over magnetite and cobalt ferrite decorated graphene oxide composite. *Plants*. 2020;10(1):6.
74. Fan T, et al. Synthesis and characterization of g-C<sub>3</sub>N<sub>4</sub>/BiFeO<sub>3</sub> composites with an enhanced visible light photocatalytic activity. *Mater Sci Semicond Process*. 2015;40:439–45.

75. Singh A. A review of wastewater irrigation: environmental implications. *Resour Conserv Recycl.* 2021;168: 105454.
76. Mfarrej MFB, et al. Floating treatment wetlands (FTWs) is an innovative approach for the remediation of petroleum hydrocarbons-contaminated water. *J Plant Growth Regul.* 2023;42(3):1402–20.

### **Publisher's Note**

Springer Nature remains neutral with regard to jurisdictional claims in published maps and institutional affiliations.